Kagome KMn$_3$Sb$_5$ metal: Magnetism, lattice dynamics, and anomalous Hall conductivity

Sobhit Singh[*]

Department of Mechanical Engineering, University of Rochester, Rochester, New York 14627, USA

A. C. Garcia-Castro [†]

School of Physics, Universidad Industrial de Santander, Carrera 27 Calle 09, 680002, Bucaramanga, Colombia

Kagome metals are reported to exhibit remarkable properties, including superconductivity, charge density wave order, and a large anomalous Hall conductivity, which facilitate the implementation of spintronic devices. In this work, we study a kagome metal based on Mn magnetic sites in a KMn$_3$Sb$_5$ stoichiometry. By means of first-principles density functional theory calculations, we demonstrate that the studied compound is dynamically stable, locking the ferromagnetic order as the ground state configuration, thus preventing the charge-density-wave state as reported in its vanadium-based counterpart KV$_3$Sb$_5$. Our calculations predict that KMn$_3$Sb$_5$ exhibits an out-of-plane (001) ferromagnetic response as the ground state, allowing for the emergence of topologically protected Weyl nodes near the Fermi level and nonzero anomalous Hall conductivity ($\sigma_{\alpha\beta}$) in this centrosymmetric system. We obtain a tangible $\sigma_{xy} = 314$ S cm^{-1} component, which is comparable to that of other kagome metals. Finally, we explore the effect of the on-site Coulomb repulsion ($+U$) on the structural and electronic properties. We observed a switching of the magnetic moment from the z axis to the x axis, for U values larger than 1.0 eV. Thus, we find that, although the lattice parameters, magnetic moment, and $\sigma_{\alpha\beta}$ moderately vary with increasing $+U$, KMn$_3$Sb$_5$ stands as an ideal stable ferromagnetic kagome metal with a tangible anomalous Hall conductivity response.

I. INTRODUCTION

Kagome lattices [1], such as those observed in FeSn [2], Co$_3$Sn$_2$S$_2$ [3], ScV$_6$Sn$_6$ [4], and the ones present in Mn$_3$$B$N ($B$ = Ni, Ga, Pt, Pd, and Sn) and V$_3$AuN antiperovskites [5–10], exhibit remarkable electronic, phononic, topological, and magnetic entangled properties, mainly owing to their particular star-shaped hexagonal symmetry [11]. In such symmetry, triangularly coordinated magnetically active cations present substantial magnetic and electronic frustration that leads, for example, to charge-density waves (CDW) phases [12], superconductivity [13] and chiral noncollinear magnetic orderings [11]. Belonging to the kagome materials, the AV$_3$Sb$_5$ (A = K, Rb, and Cs) family has recently attracted tremendous attention due to the richness of their CDW states, giant anomalous Hall response, frustrated electronic structure, and associated superconductivity [14–19]. The reported CDW phase in AV$_3$Sb$_5$ metals is originated by the electronic frustration in the in-plane vanadium sites, due to the unbalanced charge based on the expected nominal charges, i.e., K:1+, V:(5-δ)+ and Sb:3−, to enforce the charge neutrality with K^{1+}V$_3^{(5-\delta)+}$Sb$_5^{3-}$ [14]. Moreover, ferromagnetic and noncollinear antiferromagnetic states can be expected to stabilize in this family of materials, leading to tangible topological features related to Dirac and Weyl fermions in the vicinity of the Fermi level, resulting in nonvanishing Berry curvature

induced observables such as anomalous Hall conductivity (AHC) and nonlinear Hall effects [20–24]. Importantly, the electrical manipulation of Berry curvature-induced anomalous Hall effect at room temperature offers unimaginable capabilities in future spintronic devices [3,25–27]. In ferromagnetic kagome metals, reversible magnetization can be used as an external parameter to control and switch the AHC response. Therefore, the search for novel ferromagnetic kagome materials, belonging to the AM$_3$Sb$_5$ (with A = K, Rb, Cs. M = V and Mn) stoichiometry, might lead to the discovery of novel quantum phases driven by nontrivial electronic, topological, magnetic, and superconducting properties.

In this study, we employ first-principles density functional theory (DFT) calculations to investigate the structural, vibrational, magnetic, and topological electronic properties of the kagome metal KMn$_3$Sb$_5$, which was recently predicted by Jiang *et al.* [28]. Our results reveal that, despite the inherent magnetic frustration in the kagome Mn plane, KMn$_3$Sb$_5$ exhibits a stable ferromagnetic ground state, with the magnetic easy axis oriented along the (001) direction. This ferromagnetic ground state breaks time-reversal symmetry and allows the emergence of topological Weyl nodes in this centrosymmetric crystal system, resulting in large concentrations of Berry curvature near the Weyl nodes. As a result, KMn$_3$Sb$_5$ exhibits a substantial anomalous Hall conductivity response ($\sigma_{xy} = 314$ S cm^{-1}). Incorporating the on-site Coulomb parameter $+U$ in our DFT calculations moderately affects the optimized lattice parameters, magnetic moments, phonon frequencies, and $\sigma_{\alpha\beta}$ values, but no unstable phonon modes are observed within the studied range of $+U$ parameter.

─────────
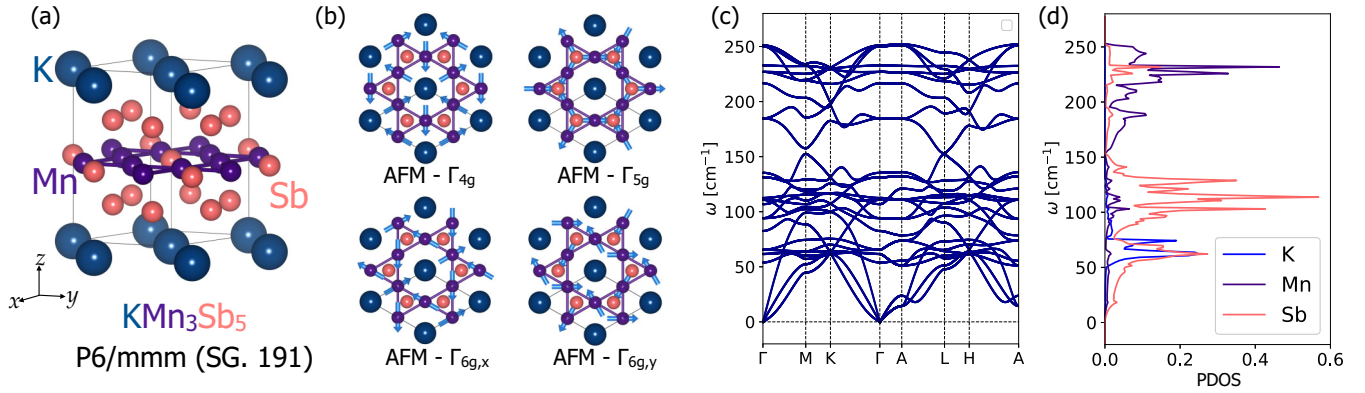[*]s.singh@rochester.edu
[†]acgarcia@uis.edu.co

FIG. 1. (a) KMn$_3$Sb$_5$ $P6/mmm$ (SG. 191) hexagonal structure obtained for the ferromagnetic, (001) FM, ground state. In this structure, the K, Mn, and Sb sites are drawn in dark blue, violet, and pink colors, respectively. (b) Chiral noncollinear antiferromagnetic orderings allowed in KMn$_3$Sb$_5$. Here, the Γ_{4g} and Γ_{5g} AFM orders hold $+1$ magnetic chirality whereas the $\Gamma_{6g,x}$ and $\Gamma_{6g,y}$ AFM orders inherit -1 magnetic chirality. (c) Phonon dispersion calculated for the ground state FM order (DFT-PBEsol). (d) Atom-projected phonon density of states.

Our findings provide valuable insights for experimentalists in synthesizing and confirming the predicted properties of the ferromagnetic kagome metal KMn$_3$Sb$_5$.

This paper is organized as follows: In Sec. II, we provide details of the computational and theoretical methods used in this study. In Sec. III, we present the results, starting with a discussion of the crystal structure and its vibrational and dynamical stability. We then analyze different magnetic configurations and explore the electronic structure, including intriguing features associated with Berry curvature and anomalous Hall conductivity. Furthermore, we examine the role of electron-correlation effects on the properties of KMn$_3$Sb$_5$. Finally, in Sec. IV, we draw our conclusions and discuss future perspectives.

II. COMPUTATIONAL DETAILS

We performed first-principles DFT calculations [29,30] using the projected-augmented wave (PAW) [31] method as implemented in the VASP code (version 5.4.4) [32,33]. The valence electron configurations considered in the PAW pseudopotentials are as follows: K: ($3p^6 4s^1$, version 02Aug2007), Mn: ($3p^6 3d^5 4s^2$, version 02Aug2007), and Sb: ($5s^2 5p^3$, version 06Sep2000). The exchange-correlation functional was computed using the generalized-gradient approximation (GGA) as parameterized by Perdew-Burke-Ernzerhof (PBS) for solids (GGA-PBEsol) [34] and the on-site correlation effects for Mn-$3d$ electrons were corrected using the rotationally invariant Liechtenstein (DFT $+ U$) formalism [35]. We used $+U$ values ranging from 0.0 to 3.0 eV, which were optimized to explore the behavior of the lattice parameters, magnetic moment, and anomalous Hall conductivity. The reciprocal space was sampled using a Γ-centered Monkhorst-Pack k mesh [36] of size $11 \times 11 \times 9$, and a kinetic energy cutoff of 600 eV was used for the plane wave basis set. These values resulted in the convergence of residual forces and total energy to better than 0.001 eV Å^{-1} and 0.1 meV. Spin-orbit coupling (SOC) was included to consider noncollinear magnetic configurations [37]. Phonon calculations were performed within the finite-differences approach [38,39] and postprocessed using the PHONOPY code [40]. To compute the

anomalous Hall conductivity and Berry curvature, we utilized the Wannier functions methodology, for which the wannierization was performed using the WANNIER90 code [41,42] and postprocessed with the WANNIERBERRI package [43]. For the wannierization process, s and p orbitals were considered for K and Sb atoms, while s, p, and d were considered for Mn atoms. To plot the Berry curvature projected on the Fermi surface, we utilized the FERMISURFER software [44]. Crystal structures were visualized using the VESTA software [45], and electronic structure data were post-processed using the PYPROCAR [46] software.

III. RESULTS AND DISCUSSION

A. Structural and Magnetic Configurations

Similar to AV$_3$Sb$_5$, KMn$_3$Sb$_5$ adopts the $P6/mmm$ (SG. 191) phase in its primitive unit cell. It consists of an Mn kagome lattice situated in the (0, 0, 1/2) plane, with several Sb sites embedded into the central kagome hexagon, as shown in Fig. 1(a). Additionally, the Mn kagome lattice is packed with graphitelike Sb layers in positions close to (0, 0, 1/4) and (0, 0, 3/4) atomic planes. Lastly, the hexagonally coordinated K atoms are located at the (0, 0, 0) sites. The DFT-optimized lattice parameters of KMn$_3$Sb$_5$ are provided below in Table II.

As a first step in the magnetic analysis, with a magnetic moment arising from the Mn sites, we define all the symmetry-allowed noncollinear magnetic states that can be

TABLE I. DFT-PBEsol calculated zone center phonon frequencies for the (001) FM ground state of KMn$_3$Sb$_5$. Data for different values of the $+U$ parameter are provided in Appendix A.

Mode	ω (cm^{-1})	Mode	ω (cm^{-1})
A_{1g}	106.8	A_{2u}	53.9, 82.5, 232.8
B_{1g}	135.3	B_{1u}	112.5, 251.1
E_{2g}	131.3	B_{2u}	216.7
E_{1g}	65.5	E_{2u}	110.7, 227.0
—	—	E_{1u}	61.6, 94.1, 184.7, 250.2

TABLE II. Lattice parameters ($a = b$, and c), magnetic moments, and $\sigma_{\alpha\beta}$ AHC component as a function of different U values in our PBEsol+U calculations. Values obtained using the meta-GGA SCAN, and r^2SCAN functionals are also listed. All the structures were fully relaxed considering the ground state (001) noncollinear ferromagnetic ordering (i.e., m_z) as well as for the (100) magnetic moment orientation (i.e., m_z). Finally, the magnetocrystalline anisotropy energy, $E_{MAE} = E_{(001)} - E_{(100)}$, is also included.

XC-type	$a = b$ (Å)	c (Å)	m_z (μ_B Mn^{-1})	σ_{xy} (S cm^{-1})	m_x (μ_B Mn^{-1})	σ_{yz} (S cm^{-1})	E_{MAE} (meV f.u.$^{-1}$)
PS + U = 0.0 eV	5.337	9.028	2.458	314	2.454	29	-0.8
PS + U = 1.0 eV	5.372	9.014	2.758	217	2.758	45	0.2
PS + U = 2.0 eV	5.470	8.875	3.312	241	3.314	193	6.9
PS + U = 3.0 eV	5.602	8.606	3.743	172	3.744	238	9.4
SCAN	5.435	9.153	3.022	—	3.026	—	6.4
r^{2}SCAN	5.512	9.042	3.229	—	3.224	—	1.3

associated with a **q** propagation vector of (0, 0, 0). We find that, similar to the case of antiperovskites [10], four xy in-plane noncollinear chiral antiferromagnetic (AFM) orderings are allowed, as shown in Fig. 1(b), along with a z axis out-of-plane ferromagnetic (FM) ordering.

We then calculated the total energies (PBEsol) for all the considered noncollinear magnetic orderings and obtained $E_{\Gamma_{4g}} = -54.0587$ eV f.u.$^{-1}$ and $E_{\Gamma_{5g}} = -54.0614$ eV f.u.$^{-1}$ for the chiral +1, and $E_{\Gamma_{6g,x}} = -54.0453$ eV f.u.$^{-1}$ and $E_{\Gamma_{6g,y}} = -54.0452$ eV f.u.$^{-1}$ for the chiral −1 orderings [47]. See Ref. [48] for more details regarding magnetic chirality. Interestingly, we find that the (001) FM state, with a total energy of $E_{FM} = -54.4928$ eV f.u.$^{-1}$ is the lowest energy magnetic ground state with an average difference energy around 500 meV f.u.$^{-1}$. This is in contrast with the observed ground state magnetic configuration in other similar materials such as the antiperovskites. In antiperovskites, the 3D kagome symmetry resolves magnetic frustration by stabilizing chiral noncollinear antiferromagnetic states instead of ferromagnetic states.

The ground state FM ordering in KMn$_3$Sb$_5$ can be explained in terms of the out-of-plane broken magnetic frustration which tends to lower the total energy compared to the strong frustrations present in the kagome lattice of antiperovskites. In antiperovskites, the kagome lattices are formed, by symmetry, in the complete ensemble of [111] family of planes, leading to the stabilization of chiral noncollinear antiferromagnetic states due to the 3D kagome symmetry. However, in KMn$_3$Sb$_5$, the out-of-plane magnetic frustration breaks this symmetry and favors the ferromagnetic ordering as the ground state magnetic configuration.

To gain a better understanding of the magnetic easy axis, we investigate the preferred direction in which the magnetic moments tend to align in the kagome plane of Mn. Specifically, we examine whether the moments lie in the xy plane (within the plane) or if they are oriented perpendicular to it (along the z axis). Our calculations (PBEsol) reveal that $E_{(100)} = -54.4920$ eV f.u.$^{-1}$ whereas $E_{(001)} = -54.4928$ eV f.u.$^{-1}$, thus implying z-axis as the easy axis for the ground state FM order in KMn$_3$Sb$_5$.

From this point on, all the reported calculations and analyses are for the (001) ferromagnetic ground state of KMn$_3$Sb$_5$. The DFT (PBEsol) optimized lattice parameters in this magnetic ground state are $a = b = 5.337$ Å and $c = 9.028$ Å.

With increasing +U value (PBEsol + U) from 0 to 3 eV on Mn-3d orbitals, primitive cell moderately expands within the a-b plane while shrinking along the c axis (see Table II) by approximately ±5%.

B. Lattice Dynamics

To test the dynamical stability of the ground state noncollinear (001) FM order in KMn$_3$Sb$_5$, we calculated the full phonon spectrum along the high-symmetry directions of the Brillouin zone, as shown in Fig. 1(c). We observe a fully stable vibrational landscape, with no unstable modes at imaginary frequencies appearing along the entire Brillouin zone. The absence of unstable phonons suggests the suppression of the charge-density-wave phenomenon induced by the unstable phonon modes, as reported in other kagome systems such as AV$_3$Sb$_5$ [15,17–19]. Thus, it is important to note that the kagome compound KMn$_3$Sb$_5$ is added to the set of materials with this symmetry, presenting potential opportunities for exhibiting a tangible ferromagnetic response. According to group theory, the irreducible representation of all allowed vibrational modes for KMn$_3$Sb$_5$ ($P6/mmm$) at Brillouin zone center is defined as follows:

$$\Gamma_{vib} = A_{1g} \oplus 4A_{2u} \oplus B_{1g} \oplus B_{1u} \oplus 2B_{2u} \oplus 2E_{2u}$$
$$\oplus E_{2g} \oplus 5E_{1u} \oplus E_{1g}. \tag{1}$$

Out of the total 27 allowed phonon modes (nine atoms per cell), the three acoustic modes are $\Gamma_{acoustic} = A_{2u} \oplus E_{1u}$, and 24 optic modes are $\Gamma_{optic} = A_{1g} \oplus 3A_{2u} \oplus B_{1g} \oplus B_{1u} \oplus 2B_{2u} \oplus 2E_{2u} \oplus E_{2g} \oplus 4E_{1u} \oplus E_{1g}$. Here, A_{1g}, E_{2g}, and E_{1g} modes are Raman active, whereas A_{2u} and E_{1u} modes are infrared (IR) active. All other modes are silent.

Table I presents the zone center phonon frequencies calculated using PBEsol ($U = 0.0$ eV) for the ground state (001) FM ordering in KMn$_3$Sb$_5$. As U is increased, the phonon frequencies vary, but no phonon instability was observed within the range of studied U values (see for example the full-phonon dispersion and the phonon DOS at $U = 3.0$ eV in Fig. 4 in Appendix A). To fully provide the behavior of the active Raman and IR frequencies, as a function of U, we present the A_{1g}, A_{2g}, and E_{1g} modes in Fig. 5(a), (in Appendix A). The A_{2u} and E_{1u} modes are presented in Fig. 5(b). In the overall trend, we can appreciate a softening of the modes when the U value is increased.
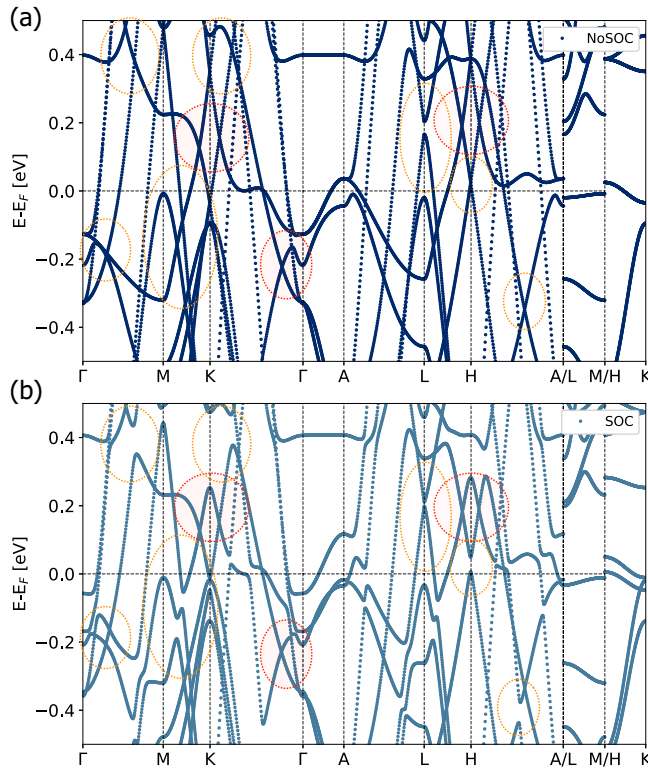
FIG. 2. Electronic band structure computed in the ferromagnetic ground state for (a) without SOC and (b) with SOC cases. For the SOC case, a (001) noncollinear ferromagnetic configuration was used. Here, in orange ovals, are marked the gapped nodes along the high-symmetry k directions whereas, in red ovals, are shown the symmetry-protected Weyl nodes. The latter are located along the M–K, and Γ–K paths at the equivalent points in the (0, 0, 1/2) plane.

Interestingly, we observe that, based on the atomically project phononic density-of-states, in Fig. 1(d), the Mn sites contribute strongly at the high-frequency modes, in between 150 to 250 cm^{-1}. On the contrary, the strongest Sb contribution can be noted between 0 cm^{-1} to 150 cm^{-1}. Finally, the K atom's contribution to the lattice dynamics is strongly localized around 60 cm^{-1}.

C. Electronic Structure

Moving forward, in Fig. 2 we present the PBEsol calculated electronic bands obtained with and without considering SOC effects. Here, it is worth recalling that noncollinear magnetic moments of Mn are aligned along the z axis. As expected, our band structure calculations reveal metallic features. We note that the inclusion of $+U$ in our DFT calculations does not result in the opening of any bandgap; it only moderately modifies the details of the bands near the Fermi level (see, for example, the electronic band dispersion obtained for $U = 3.0$ eV Fig. 6 in Appendix B).

At first glance, in the absence of SOC, we notice multiple band crossings near the Fermi level that might be associated with potential topological nodes, in Fig. 2(a). Some of these band crossings become gapped once the SOC effects are included, leading to the emergence of a

multitude of topologically protected Weyl nodes in the vicinity of these gapped band crossings and away from the high-symmetry k path considered in Fig. 2(b) [49–51]. Additionally, several crystal symmetry-protected nodes occur along the high-symmetry directions of the Brillouin zone, as expected for the kagome symmetry [3,52]. These crystal symmetry-protected nodes are located, for example, along the M–K and Γ–K k-paths at energies close to 150 meV above the Fermi level. There are symmetry-protected nodes also located at the L–H and H–A in the (0, 0, 1/2) k plane. All these Weyl nodes serve as sources and sinks of Berry curvature in the momentum space yielding a large AHC response in the FM kagome metal KMn$_3$Sb$_5$, as we discuss below. As expected, the spin-projection of the Weyl nodes is reversed, as can be appreciated from the spin-polarized electronic band structure shown in Fig. 7 at Appendix C. Here, only the S_z component is observed in the vicinity of the Fermi energy, which is in agreement with the underlying magnetic structure.

D. Anomalous Hall Conductivity

By analyzing the symmetry-allowed properties and electronic structure, we notice that the ferromagnetic kagome metal KMn$_3$Sb$_5$ may exhibit a tangible anomalous Hall conductivity (AHC) response. Consequently, in the $P6/mm'm'$ magnetic space group (MSG. 191.240), the AHC tensor ($\sigma_{\alpha\beta}$) is extracted and presented in Eq. 2. Most of the AHC tensor elements are forced to vanish due to symmetry, except for σ_{xy} and σ_{yx} which are allowed to have nonzero values. However, it is important to note that $\sigma_{yx} = -\sigma_{xy}$. Thus, the nonzero AHC components lie within the kagome plane and perpendicular to the orientation of Mn magnetic moments breaking the time-reversal symmetry:

$$\sigma_{6/mm'm'} = \begin{pmatrix} 0 & \sigma_{xy} & 0 \\ -\sigma_{xy} & 0 & 0 \\ 0 & 0 & 0 \end{pmatrix}. \qquad (2)$$

Figure 3(a) shows the variation of σ_{xy} as a function of the chemical potential near the Fermi level, calculated using the Kubo formula [53,54]. See Ref. [55] for more details. As it can be observed, the AHC at the Fermi level is $\sigma_{xy} = 314$ S cm^{-1}. This is comparable to the values obtained in similar kagome compounds with large, or even giant, AHC such as $\sigma_{xy} = 380$ S cm^{-1} in LiMn$_6$Sn$_6$ [56], $\sigma_{xy} = 1130$ S cm^{-1} in Co$_3$Sn$_2$S$_2$ [3], and $\sigma_{xy} = -400$ S cm^{-1} in Fe$_3$Sn$_2$ [57]. Notably, by tuning the Fermi level in kagome metal KMn$_3$Sb$_5$, it is possible to achieve a σ_{xy} value close to or even larger than 1000 S cm^{-1}.

In Fig. 3(b), we present the Berry curvature components Ω_x, Ω_y, and Ω_z calculated along the high-symmetry directions in the Brillouin zone. The largest contributions to the Berry curvature are obtained for Ω_z at the H point and along the H–K path. The values extend up to -7000 Å^2, though in Fig. 3(b), the y axis is displayed only up to -1000 Å^2 to allow for the observation of smaller contributions along the other Brillouin zone paths. By correlating the Berry curvature with the electronic band structure calculated with SOC, we notice that there is a SOC-induced gapped node at the H point near the Fermi energy (see Fig. 2), suggesting the presence of
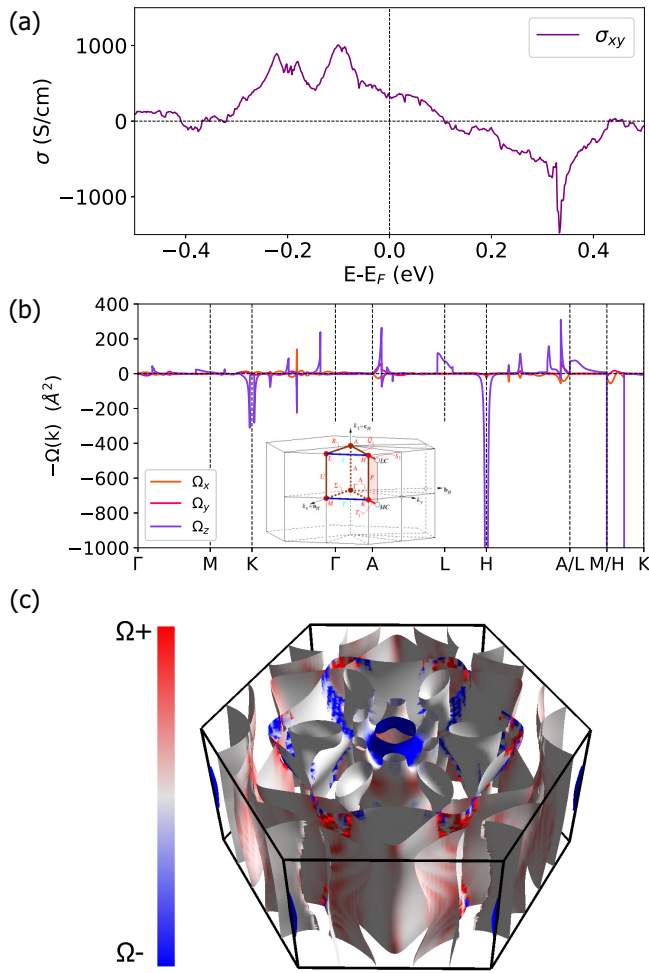
FIG. 3. (a) Anomalous Hall conductivity, σ_{xy} component, calculated (PBEsol) as a function of the chemical potential near the Fermi energy (E_F) for the ferromagnetic (001) KMn₃Sb₅ within the $P6/mm'm'$ magnetic space group (MSG. 191.240). (b) Berry curvature, $\Omega_x(k)$, $\Omega_y(k)$, and $\Omega_z(k)$ components, calculated using DFT-PBEsol and integrated along the Brillouin zone k path. In the inset, we display the hexagonal Brillouin zone for the SG. 191 space group in which, the high-symmetry points and relevant k paths are marked. (c) $\Omega_z(\mathbf{k})$ component of Berry curvature projected onto the Fermi surface of ferromagnetic (001) KMn₃Sb₅ using a color map. Blue and red colors denote the negative and positive components of $\Omega_z(\mathbf{k})$, respectively.

potential gapless Weyl nodes in the vicinity of the H point. This explains the divergent Berry curvature at the Weyl nodes [58] which are the main source of the large AHC response in KMn₃Sb₅. Similar behavior has also been reported in antiperovskite compounds such as Mn₃NiN and V₃AuN [8,10]. Fig. 3(b) also displays the hexagonal Brillouin zone obtained for $P6/mmm$ space group in which, the high-symmetry points and relevant k paths are marked. Figure 3(c) shows the calculated Berry curvature $\Omega_z(\mathbf{k})$ projected onto the Fermi surface of KMn₃Sb₅. Here, the red and blue colors denote the positive and negative $\Omega_z(\mathbf{k})$ values. Throughout the entire Brillouin zone, multiple strong concentrations of Berry curvature can be observed.

E. Role of Electronic Correlations

As shown in previous reports [9,59–61], the kagome lattices with magnetic cations, especially cations having partially-filled $3d$ valence shell, exhibit strong electronic-correlation phenomenon that leads to the emergence of exciting electronic properties. Therefore, to investigate the effects of the on-site Coulomb interaction on Mn-$3d$ electrons and its impact on the structural, phononic, and electronic properties, we employed DFT+U calculations which capture the electronic-correlations effects at the mean-field level [35]. This analysis is particularly important due to the lack of experimental reports on KMn₃Sb₅, and it may help experimentalists in identifying suitable observables for future investigations.

In Table II, we present the evolution of the lattice parameters, the magnetic moment per Mn atom, anomalous Hall conductivity, and the magnetocrystalline anisotropy energy values as a function of the +U Coulomb correction parameter applied to Mn-$3d$ electrons. Our results reveal an increase in the in-plane lattice parameters (i.e., $a = b$) while a decrease in the out-of-plane (i.e., c) lattice parameter with increasing U. This demonstrates the dominant role of the Mn–Mn bondings and interactions within the kagome lattice. The observed expansion in the in-plane lattice parameters is in agreement with the previous observation of the strong spin-lattice coupling related to the negative thermal expansion in the kagome antiperovskite Mn₃NiN [9]. It is worth noting that with increasing U value, some phonon modes (especially the in-plane vibrational modes) soften due to the increased in-plane lattice parameters. However, no unstable phonon modes are observed within the range of considered U values. Regarding the magnetic structure, we observed that the magnetic easy-axis is flipped from the kagome out-of-plane z axis to the in-plane x axis for values of U larger than 1.0 eV. Therefore, in Table II we condensed the results obtained when the magnetic moment is aligned along the z axis as well as along the x axis. As expected, the magnetic moment per Mn-site is increased, for both m_z and m_x cases, due to the increased electron localization governed by the Coulomb term. As for the magnetic symmetry, once the in-plane x-axis magnetization is considered, the magnetic symmetry group lies in the $Cmm'm'$ (MGS. 65.486). Under this symmetry condition, the nonzero anomalous Hall conductivity is expressed as follows:

$$\sigma_{mm'm'} = \begin{pmatrix} 0 & 0 & 0 \\ 0 & 0 & \sigma_{yz} \\ 0 & -\sigma_{yz} & 0 \end{pmatrix}. \tag{3}$$

Interestingly, the σ_{xy} in Table II component remains substantial at all the considered U values, meanwhile the σ_{yz}, also presented in Table II, increase as a function of U. Finally, we fully relax the KMn₃Sb₅ structure in the FM (001) ordering, as well as the FM (100) magnetic structure by using the meta-GGA SCAN [62] and r² SCAN [63] functionals. This aims to obtain more precise values of the interesting observables. We find that the magnetic moments, for both m_z and m_z cases are close to $3.02\,\mu_B\,\mathrm{Mn}^{-1}$ and $3.22\,\mu_B\,\mathrm{Mn}^{-1}$ for the SCAN and r² SCAN functionals, respectively. Moreover, the relaxed

lattice parameters are $a = 5.435$ Å and $c = 9.153$ Å for the SCAN functional whereas $a = 5.512$ Å and $c = 9.042$ Å for the r^2 SCAN functional in which, no substantial changes were observed when the structure is relaxed under the FM (001) and FM (100) orderings. In terms of the E_{MAE} our calculations suggest that the in-plane ferromagnetic ordering is the lowest energy state when the meta-GGA approach is considered. Using these meta-GGA values as observables, we might suggest that a U value around 2.0 eV could reasonably reproduce the structural and electronic properties of KMn$_3$Sb$_5$. Nonetheless, more theoretical and experimental efforts are needed to corroborate these findings. Moreover, it is important to note that more systematic studies are needed to fully comprehend the electron-correlation effects in this studied strongly correlated kagome metal.

IV. CONCLUSIONS

In this study, we performed comprehensive first-principles DFT calculations to investigate the properties of the novel Mn-based kagome metal KMn$_3$Sb$_5$. Our results indicate that KMn$_3$Sb$_5$ is both structurally and vibrationally stable, with no observed unstable phonon modes. This is in contrast to the KV$_3$Sb$_5$ compound, in which phonon instability leads to the appearance of CDW phase. A detailed investigation of the possible candidate magnetic configurations (noncollinear FM as well as AFM) reveal the (001) ferromagnetic ordering, in absence of on-site U Coulomb correction, as the ground state in KMn$_3$Sb$_5$, although various other magnetically frustrated kagome metals favor noncollinear chiral antiferromagnetic orderings Γ_{4g} and Γ_{5g}, similar to the case of Mn$_3$NiN antiperovskite, due to the inherent magnetic frustration. The electronic structure shows multiple nodal crossings associated with Weyl nodes near the Fermi energy, indicating topologically nontrivial features present in the studied material. Notably, the ferromagnetic order breaks the time-reversal symmetry, resulting in a tangible anomalous Hall conductivity response. We find a value of $\sigma_{xy} = 314$ S cm^{-1}, which moderately varies with increasing on-site Coulomb parameter U in our PBEsol+U calculations. We find that the predicted σ_{xy} in KMn$_3$Sb$_5$ to be considerably large when compared to other similar kagome compounds. Interestingly, we observed a flipping of the magnetic moment, forming the z axis to the x axis, for on-site Coulomb values larger than 1.0 eV. Nonetheless, the AHC is also present with an σ_{yz} that is increased as a function of the U value. We suggest a U value around 2.0 eV might reasonably reproduce the properties of the ferromagnetic kagome metal KMn$_3$Sb$_5$. Our findings are expected to motivate experimentalists to pursue the synthesis, realization, and subsequent confirmation of the predicted properties in KMn$_3$Sb$_5$.

ACKNOWLEDGMENTS

APPENDIX A: PHONONS UNDER THE +U CORRECTION

Appendix A includes the phonon dispersion curves and the phonon density of states computed at +U value of
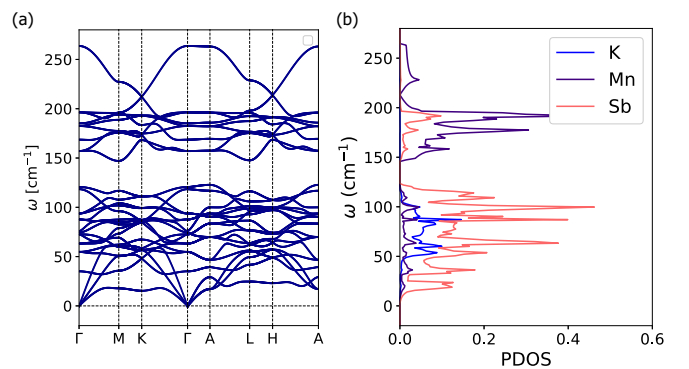

FIG. 4. (a) Full phonon-dispersion curve and (b) Atom-projected phonon density of states obtained at the Coulomb +U value of 3.0 eV as a correction in the $3d$:Mn states at the KMn$_3$Sb$_5$ kagome compound.
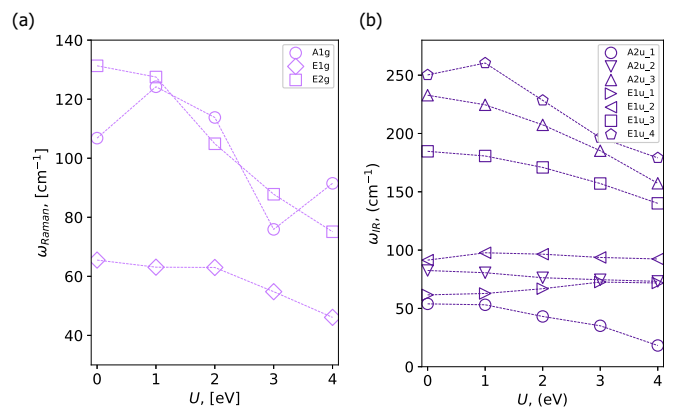

FIG. 5. BZ zone center Raman and IR active modes as a function of the +U parameter in the KMn$_3$Sb$_5$.
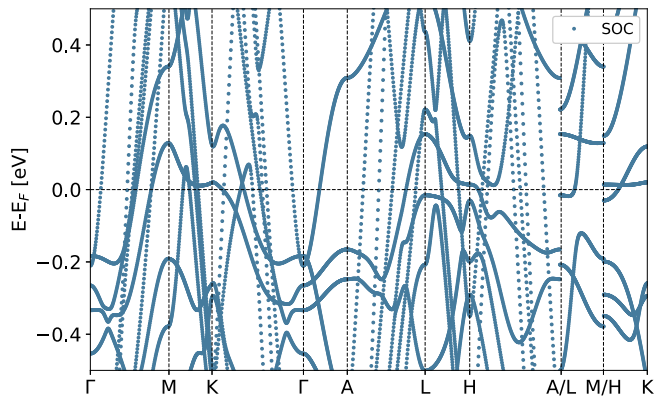
FIG. 6. (a) Full dispersion bands obtained at the Coulomb $+U$ value of 3.0 eV as a correction in the $3d$:Mn states at the KMn$_3$Sb$_5$ kagome compound.

3.0 eV where the dynamical stability of the kagome compound holds for large Coulomb $+U$ values. Additionally, the zone-center phonon frequencies are included as a function of the U values, ranging from 0.0 eV to 4.0 eV.

APPENDIX B: ELECTRONIC BANDS UNDER THE $+U$ CORRECTION

Appendix B presents the electronic band structure obtained for the $+U$ value of 3.0 eV.

APPENDIX C: SPIN-POLARIZED BAND STRUCTURE

Appendix C presents the spin-projected band structure, in the absence of $+U$ correction, obtained for the kagome KMn$_3$Sb$_5$. As it can be observed, only S_z spin projection is obtained in agreement with the (001) ferromagnetic ordering.
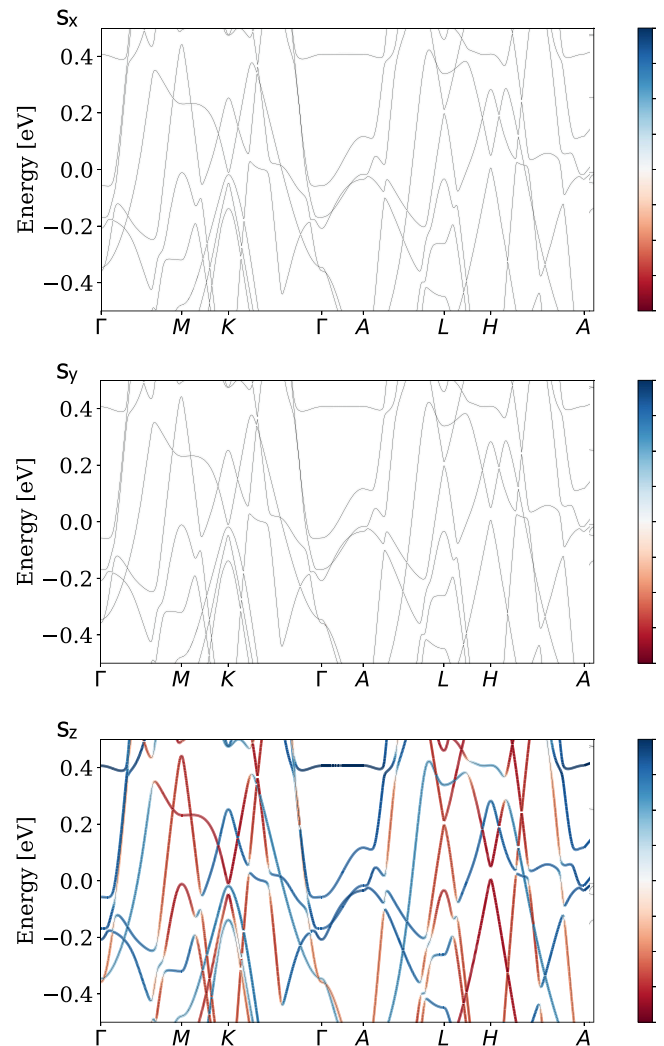

FIG. 7. Spin-polarized electronic band structure showing the S_x, S_y, and S_z spin components, respectively. Here, it can be noted that the contributions from the S_x and S_y spin projections are negligible, and only, the S_z component is appreciated in the E$_F$ proximity. Additionally, the Weyl nodes can be identified in the path between the M–K and K–Γ points and consequently, in the associated point, L–H and H–A in the (0, 0, 1/2) plane. Here, the blue and red colors denote the up- and down-spin projections, respectively.

[1] M. Mekata, Kagome: The story of the basket weave lattice, Phys. Today **56**, 12 (2003).

[2] M. Kang, L. Ye, S. Fang, J.-S. You, A. Levitan, M. Han, J. I. Facio, C. Jozwiak, A. Bostwick, E. Rotenberg, M. K. Chan, R. D. McDonald, D. Graf, K. Kaznatcheev, E. Vescovo, D. C. Bell, E. Kaxiras, J. van den Brink, M. Richter, M. Prasad Ghimire *et al.*, Dirac fermions and flat bands in the ideal kagome metal FeSn, Nat. Mater. **19**, 163 (2020).

[3] E. Liu, Y. Sun, N. Kumar, L. Muechler, A. Sun, L. Jiao, S.-Y. Yang, D. Liu, A. Liang, Q. Xu, J. Kroder, V. Süß, H. Borrmann, C. Shekhar, Z. Wang, C. Xi, W. Wang, W. Schnelle, S. Wirth,

Y. Chen *et al.*, Giant anomalous Hall effect in a ferromagnetic kagome-lattice semimetal, Nat. Phys. **14**, 1125 (2018).

[4] H. W. S. Arachchige, W. R. Meier, M. Marshall, T. Matsuoka, R. Xue, M. A. McGuire, R. P. Hermann, H. Cao, and D. Mandrus, Charge density wave in kagome lattice intermetallic ScV$_6$Sn$_6$, Phys. Rev. Lett. **129**, 216402 (2022).

[5] Y. Wang, H. Zhang, J. Zhu, X. Lü, S. Li, R. Zou, and Y. Zhao, Antiperovskites with exceptional functionalities, Adv. Mater. **32**, 1905007 (2019).

[6] A. C. Garcia-Castro, R. Ospina, and J. H. Quintero, Octahedral distortion and electronic properties of the antiperovskite

oxide Ba$_3$SiO: First principles study, J. Phys. Chem. Solids **136**, 109126 (2020).

[7] A. C. Garcia-Castro, J. H. Quintero Orozco, and C. J. Paez Gonzalez, Hybrid-improper ferroelectric behavior in Ba$_3$SiO/Ba$_3$GeO oxide antiperovskite superlattices, Eur. Phys. J. B **92**, 203 (2019).

[8] D. Torres-Amaris, A. Bautista-Hernandez, R. González-Hernández, A. H. Romero, and A. C. Garcia-Castro, Anomalous Hall conductivity control in Mn$_3$NiN antiperovskite by epitaxial strain along the kagome plane, Phys. Rev. B **106**, 195113 (2022).

[9] L. Flórez-Gómez, W. Ibarra-Hernández, and A. Garcia-Castro, Lattice dynamics and spin-phonon coupling in the noncollinear antiferromagnetic antiperovskite Mn$_3$NiN, J. Magn. Magn. Mater. **562**, 169813 (2022).

[10] J. M. Duran-Pinilla, A. H. Romero, and A. C. Garcia-Castro, Chiral magnetism, lattice dynamics, and anomalous hall conductivity in V$_3$AuN antiferromagnetic antiperovskite, Phys. Rev. Mater. **6**, 125003 (2022).

[11] N. J. Ghimire and I. I. Mazin, Topology and correlations on the kagome lattice, Nat. Mater. **19**, 137 (2020).

[12] J. Luo, Z. Zhao, Y. Z. Zhou, J. Yang, A. F. Fang, H. T. Yang, H. J. Gao, R. Zhou, and G.-q. Zheng, Possible star-of-david pattern charge density wave with additional modulation in the kagome superconductor CsV$_3$Sb$_5$, npj Quantum Mater. **7**, 30 (2022).

[13] J.-X. Yin, B. Lian, and M. Z. Hasan, Topological kagome magnets and superconductors, Nature (London) **612**, 647 (2022).

[14] B. R. Ortiz, L. C. Gomes, J. R. Morey, M. Winiarski, M. Bordelon, J. S. Mangum, I. W. H. Oswald, J. A. Rodriguez-Rivera, J. R. Neilson, S. D. Wilson, E. Ertekin, T. M. McQueen, and E. S. Toberer, New kagome prototype materials: Discovery of KV$_3$Sb$_5$, RbV$_3$Sb$_5$, and CsV$_3$Sb$_5$, Phys. Rev. Mater. **3**, 094407 (2019).

[15] D. Subires, A. Korshunov, A. H. Said, L. Sánchez, B. R. Ortiz, S. D. Wilson, A. Bosak, and S. Blanco-Canosa, Order-disorder charge density wave instability in the kagome metal (Cs,Rb)V$_3$Sb$_5$, Nat. Commun. **14**, 1015 (2023).

[16] E. Uykur, B. R. Ortiz, S. D. Wilson, M. Dressel, and A. A. Tsirlin, Optical detection of the density-wave instability in the kagome metal KV$_3$Sb$_5$, npj Quantum Mater. **7**, 16 (2022).

[17] E. T. Ritz, R. M. Fernandes, and T. Birol, Impact of Sb degrees of freedom on the charge density wave phase diagram of the kagome metal CsV$_3$Sb$_5$, Phys. Rev. B **107**, 205131 (2023).

[18] E. Ritz, H. S. Røising, M. H. Christensen, T. Birol, B. M. Andersen, and R. M. Fernandes, Superconductivity from orbital-selective electron-phonon coupling in AV$_3$Sb$_5$, Phys. Rev. B **108**, L100510 (2023).

[19] A. Ptok, A. Kobiałka, M. Sternik, J. Łażewski, P. T. Jochym, A. M. Oleś, and P. Piekarz, Dynamical study of the origin of the charge density wave in AV3Sb5 (A=K, Rb, Cs) compounds, Phys. Rev. B, **105**, 235134, (2022).

[20] H. Chen, Q. Niu, and A. H. MacDonald, Anomalous Hall effect arising from noncollinear antiferromagnetism, Phys. Rev. Lett. **112**, 017205 (2014).

[21] L. Šmejkal, A. H. MacDonald, J. Sinova, S. Nakatsuji, and T. Jungwirth, Anomalous Hall antiferromagnets, Nat. Rev. Mater. **7**, 482 (2022).

[22] X. Wang, D. Vanderbilt, J. R. Yates, and I. Souza, Fermi-surface calculation of the anomalous Hall conductivity, Phys. Rev. B **76**, 195109 (2007).

[23] X. Wang, J. R. Yates, I. Souza, and D. Vanderbilt, *Ab initio* calculation of the anomalous Hall conductivity by wannier interpolation, Phys. Rev. B **74**, 195118 (2006).

[24] S. Singh, J. Kim, K. M. Rabe, and D. Vanderbilt, Engineering weyl phases and nonlinear Hall effects in T$_d$-MoTe$_2$, Phys. Rev. Lett. **125**, 046402 (2020).

[25] H. Tsai, T. Higo, K. Kondou, T. Nomoto, A. Sakai, A. Kobayashi, T. Nakano, K. Yakushiji, R. Arita, S. Miwa, Y. Otani, and S. Nakatsuji, Electrical manipulation of a topological antiferromagnetic state, Nature (London), **580**, 608 (2020).

[26] P. X. Qin, H. Yan, X. N. Wang, Z. X. Feng, H. X. Guo, X. R. Zhou, H. J. Wu, X. Zhang, Z. G. G. Leng, H. Y. Chen, and Z. Q. Liu, Noncollinear spintronics and electric-field control: A review, Rare Metals, **39**, 95 (2019).

[27] H. Bai, Y. C. Zhang, L. Han, Y. J. Zhou, F. Pan, and C. Song, Antiferromagnetism: An efficient and controllable spin source, Appl. Phys. Rev. **9**, 041316 (2022).

[28] Y. Jiang, Z. Yu, Y. Wang, T. Lu, S. Meng, K. Jiang, and M. Liu, Screening promising CsV$_3$Sb$_5$-like kagome materials from systematic first-principles evaluation, Chin. Phys. Lett. **39**, 047402 (2022).

[29] P. Hohenberg and W. Kohn, Inhomogeneous electron gas, Phys. Rev. **136**, B864 (1964).

[30] W. Kohn and L. J. Sham, Self-consistent equations including exchange and correlation effects, Phys. Rev. **140**, A1133 (1965).

[31] P. E. Blöchl, Projector augmented-wave method, Phys. Rev. B **50**, 17953 (1994).

[32] G. Kresse and J. Furthmüller, Efficient iterative schemes for *ab initio* total-energy calculations using a plane-wave basis set, Phys. Rev. B **54**, 11169 (1996).

[33] G. Kresse and D. Joubert, From ultrasoft pseudopotentials to the projector augmented-wave method, Phys. Rev. B **59**, 1758 (1999).

[34] J. P. Perdew, A. Ruzsinszky, G. I. Csonka, O. A. Vydrov, G. E. Scuseria, L. A. Constantin, X. Zhou, and K. Burke, Restoring the density-gradient expansion for exchange in solids and surfaces, Phys. Rev. Lett. **100**, 136406 (2008).

[35] A. I. Liechtenstein, V. I. Anisimov, and J. Zaanen, Density-functional theory and strong interactions: Orbital ordering in Mott-Hubbard insulators, Phys. Rev. B **52**, R5467 (1995).

[36] H. J. Monkhorst and J. D. Pack, Special points for brillouin-zone integrations, Phys. Rev. B **13**, 5188 (1976).

[37] D. Hobbs, G. Kresse, and J. Hafner, Fully unconstrained noncollinear magnetism within the projector augmented-wave method, Phys. Rev. B **62**, 11556 (2000).

[38] K. Kunc and R. M. Martin, *Ab initio* force constants of GaAs: A new approach to calculation of phonons and dielectric properties, Phys. Rev. Lett. **48**, 406 (1982).

[39] P. K. Lam, M. M. Dacorogna, and M. L. Cohen, Self-consistent calculation of electron-phonon couplings, Phys. Rev. B **34**, 5065 (1986).

[40] A. Togo and I. Tanaka, First principles phonon calculations in materials science, Scr. Mater. **108**, 1 (2015).

[41] A. A. Mostofi, J. R. Yates, G. Pizzi, Y.-S. Lee, I. Souza, D. Vanderbilt, and N. Marzari, An updated version of WANNIER90:

A tool for obtaining maximally-localised Wannier functions, Comput. Phys. Commun. **185**, 2309 (2014).

[42] G. Pizzi, V. Vitale, R. Arita, S. Blügel, F. Freimuth, G. Géranton, M. Gibertini, D. Gresch, C. Johnson, T. Koretsune, J. Ibañez-Azpiroz, H. Lee, J.-M. Lihm, D. Marchand, A. Marrazzo, Y. Mokrousov, J. I. Mustafa, Y. Nohara, Y. Nomura, L. Paulatto *et al.*, Wannier90 as a community code: New features and applications, J. Phys.: Condens. Matter **32**, 165902 (2020).

[43] S. S. Tsirkin, High performance Wannier interpolation of Berry curvature and related quantities with Wannier Berri code, npj Comput. Mater. **7**, 33 (2021).

[44] M. Kawamura, Fermisurfer: Fermi-surface viewer providing multiple representation schemes, Comput. Phys. Commun. **239**, 197 (2019).

[45] K. Momma and F. Izumi, *VESTA3* for three-dimensional visualization of crystal, volumetric and morphology data, J. Appl. Crystallogr. **44**, 1272 (2011).

[46] U. Herath, P. Tavadze, X. He, E. Bousquet, S. Singh, F. Muñoz, and A. H. Romero, PyProcar: A python library for electronic structure pre/post-processing, Comput. Phys. Commun. **251**, 107080 (2020).

[47] H. Kawamura and S. Miyashita, Phase transition of the two-dimensional Heisenberg antiferromagnet on the triangular lattice, J. Phys. Soc. Jpn. **53**, 4138 (1984).

[48] The magnetic vector chirality is defined as $\kappa = \frac{2}{3\sqrt{3}} \sum_{i,j} (\mathbf{S}_i \times \mathbf{S}_j)$ $= \frac{2}{3\sqrt{3}} (\mathbf{S}_1 \times \mathbf{S}_2 + \mathbf{S}_2 \times \mathbf{S}_3 + \mathbf{S}_3 \times \mathbf{S}_1)$ for the kagome lattice where the i and j index run over the magnetic moments in the unit cell.

[49] L. Ye, M. Kang, J. Liu, F. von Cube, C. R. Wicker, T. Suzuki, C. Jozwiak, A. Bostwick, E. Rotenberg, D. C. Bell, L. Fu, R. Comin, and J. G. Checkelsky, Massive Dirac fermions in a ferromagnetic kagome metal, Nature (London) **555**, 638 (2018).

[50] S. Singh, A. C. Garcia-Castro, I. Valencia-Jaime, F. Muñoz, and A. H. Romero, Prediction and control of spin polarization in a Weyl semimetallic phase of BiSb, Phys. Rev. B **94**, 161116(R) (2016).

[51] B. Karki, B. P. Belbase, G. B. Acharya, S. Singh, and M. P. Ghimire, Pressure-induced creation and annihilation of Weyl points in $T_d-\text{Mo}_{0.5}\text{W}_{0.5}\text{Te}_2$ and $1T''-\text{Mo}_{0.5}\text{W}_{0.5}\text{Te}_2$, Phys. Rev. B **105**, 125138 (2022).

[52] L. Muechler, E. Liu, J. Gayles, Q. Xu, C. Felser, and Y. Sun, Emerging chiral edge states from the confinement of a magnetic Weyl semimetal in Co$_3$Sn$_2$S$_2$, Phys. Rev. B **101**, 115106 (2020).

[53] R. Kubo, Statistical-mechanical theory of irreversible processes. I. general theory and simple applications to magnetic and conduction problems, J. Phys. Soc. Jpn. **12**, 570 (1957).

[54] A. Crépieux and P. Bruno, Theory of the anomalous hall effect from the Kubo formula and the Dirac equation, Phys. Rev. B **64**, 014416 (2001).

[55] The anomalous Hall conductivity component, $\sigma_{\alpha\beta}$, has been computed by following the relationship:

$$\sigma_{\alpha\beta} = -\frac{e^2}{\hbar} \sum_{n}^{occ} \int_{BZ} \frac{d^3k}{(2\pi)^3} f_n(\mathbf{k})\Omega_{n,\alpha\beta}(\mathbf{k}), \quad (\text{C1})$$

where $\Omega_{\alpha\beta}(\mathbf{k}) = \sum_{n}^{occ} f_n(\mathbf{k})\mathbf{\Omega}_{\mathbf{n},\alpha\beta}(\mathbf{k})$ corresponds to the Berry curvature in the $\alpha\beta$ plane and it is the result of the summation of all the occupied n bands and $f_n(\mathbf{k})$ represents the Fermi distribution. In this calculations, the $\Omega_{n,\alpha\beta}(\mathbf{k})$ Berry curvature is estimated such as:

$$\Omega_{n,\alpha\beta}(\mathbf{k}) = -2i\hbar^2 \sum_{m\neq n} \frac{\langle \psi_{n,\mathbf{k}}|v_\alpha|\psi_{m,\mathbf{k}}\rangle \langle \psi_{m,\mathbf{k}}|v_\beta|\psi_{n,\mathbf{k}}\rangle}{[E_m(\mathbf{k}) - E_n(\mathbf{k})]^2}. \quad (\text{C2})$$

In the latter equation, $\psi_{n,\mathbf{k}}$ and v_α, v_β are the Bloch functions and the velocity operators, respectively. In this step, an $320 \times 320 \times 320\,k$ mesh was used.

[56] D. Chen, C. Le, C. Fu, H. Lin, W. Schnelle, Y. Sun, and C. Felser, Large anomalous Hall effect in the kagome ferromagnet LiMn$_6$Sn$_6$, Phys. Rev. B **103**, 144410 (2021).

[57] Q. Wang, S. Sun, X. Zhang, F. Pang, and H. Lei, Anomalous hall effect in a ferromagnetic Fe$_3$Sn$_2$ single crystal with a geometrically frustrated Fe bilayer kagome lattice, Phys. Rev. B **94**, 075135 (2016).

[58] D. Xiao, M.-C. Chang, and Q. Niu, Berry phase effects on electronic properties, Rev. Mod. Phys. **82**, 1959 (2010).

[59] M. Y. Jeong, H.-J. Yang, H. S. Kim, Y. B. Kim, S. B. Lee, and M. J. Han, Crucial role of out-of-plane Sb p orbitals in van hove singularity formation and electronic correlations in the superconducting kagome metal CsV$_3$Sb$_5$, Phys. Rev. B **105**, 235145 (2022).

[60] D. Di Sante, B. Kim, W. Hanke, T. Wehling, C. Franchini, R. Thomale, and G. Sangiovanni, Electronic correlations and universal long-range scaling in kagome metals, Phys. Rev. Res. **5**, L012008 (2023).

[61] X. Wu, T. Schwemmer, T. Müller, A. Consiglio, G. Sangiovanni, D. Di Sante, Y. Iqbal, W. Hanke, A. P. Schnyder, M. M. Denner, M. H. Fischer, T. Neupert, and R. Thomale, Nature of unconventional pairing in the kagome superconductors AV$_3$Sb$_5$ (A = K, Rb, Cs), Phys. Rev. Lett. **127**, 177001 (2021).

[62] J. Sun, A. Ruzsinszky, and J. P. Perdew, Strongly constrained and appropriately normed semilocal density functional, Phys. Rev. Lett. **115**, 036402 (2015).

[63] J. W. Furness, A. D. Kaplan, J. Ning, J. P. Perdew, and J. Sun, Accurate and numerically efficient r^{2}SCAN meta-generalized gradient approximation, J. Phys. Chem. Lett. **11**, 8208 (2020).